Molecular Mechanisms of Holliday Junction Branch Migration Catalyzed by an Asymmetric RuvB Hexamer

Anthony D. Rish[1,2,3,5], Zhangfei Shen[2,3,5], Zhenhang Chen[2, 3,4], Tian-Min Fu[1,2,3,*]

[1]The Ohio State Biochemistry Program, The Ohio State University, Columbus, OH 43210, USA.

[2]Department of Biological Chemistry and Pharmacology, The Ohio State University, Columbus, OH 43210, USA.

[3]The Ohio State University Comprehensive Cancer Center, Columbus, OH 43210, USA.

[4]Current address: Department of Biochemistry, Emory University School of Medicine, Atlanta, GA 30322, USA.

[5]These authors contributed equally to this work.

*Correspondence should be addressed to: fu.978@osu.edu.

ABSTRACT

The Holliday junction (HJ) is a universal DNA intermediate of homologous recombination that is involved in many fundamental physiological processes. In bacteria, RuvB, a motor protein of the AAA^+ ATPase superfamily, drives branch migration of the Holliday junction with a mechanism that had yet to be elucidated. Here, we report two cryo-EM structures of RuvB in complex with DNA and nucleotides, providing a comprehensive understanding of HJ branch migration. Six RuvB protomers assemble into a spiral staircase, in the shape of a ring, with DNA in the central pore. Four protomers of RuvB hexamer interact with the backbone of the DNA substrate, suggesting a pulling-and-revolving mechanism of DNA translocation with a basic step size of 2 nucleotides. Moreover, the variation of nucleotide-binding states in our RuvB hexamer supports a sequential model for ATP hydrolysis, ADP release, and ATP reloading, which occur at specific positions on the RuvB hexamer. Furthermore, the asymmetric assembly of RuvB also explains the 6:4 stoichiometry between RuvB and RuvA, which assembles into a complex to coordinate HJ migration in cells. Taken together, we provide a comprehensive framework for the mechanistic understanding of HJ branch migration facilitated by RuvB motor protein, which may be universally shared in both prokaryotic and eukaryotic organisms.

INTRODUCTION

Homologous recombination is an omnipresent cellular process that is critical not just for the maintenance of genomic stability after DNA damage, but also for generating genetic diversity and has been associated with a variety of human diseases[1]. After DNA damage is detected, a series of steps including strand invasion and D-loop formation occur before a key intermediate structure of homologous recombination, the Holliday junction (HJ), is formed[2]. The HJ consists of two double-stranded DNA (dsDNA) helices that are separated into four hetero-duplex strands through a crossover point. In bacteria, RuvA, RuvB, and RuvC are involved in processing the HJ. RuvA was shown to assemble into a tetramer for recognizing the HJ core and recruits RuvB, a motor protein, to facilitate branch migration of the HJ. Eventually, the HJ is resolved back into two complete DNA strands by RuvC, an endonuclease. In eukaryotes, there are homologous proteins of the RuvAB complex, such as Rad54 in humans, to conduct HJ branch migration[3-6]. Therefore, fundamental mechanisms of HJ migration in bacteria may be universally shared by all organisms.

Earlier structural studies have provided rich information regarding interactions of RuvA with HJ DNA and RuvB. RuvA has been shown to consist of three distinct domains (Domain I, II, and III). A crystal structure of RuvA in complex with HJ has revealed that RuvA forms a unique tetrameric architecture, in which domains I and II are responsible for Holliday junction binding[7]. Domain III of RuvA was shown to directly interact with RuvB for loading of RuvB onto HJ[8]. Crystal structures of RuvB from different bacteria showed that RuvB shares a conserved architecture that is composed of three domains: N-terminal domain ($RuvB^N$), Middle domain ($RuvB^M$), and C-terminal Domain ($RuvB^C$)[9-11]. A feature **β**-hairpin in $RuvB^N$ was shown to interact with domain III of RuvA through hydrophobic interactions[8].

RuvB belongs to the AAA^+ (ATPase associated with various cellular activity) family, which includes many members involved in numerous physiological processes[12]. All AAA^+ proteins share a core domain with an **αβα** sandwich-fold, which contains two key motifs, the Walker A motif and the Walker B motif[13]. Walker A motif is composed of GXXXGK(T/S), where x stands for any amino acid, and the Walker B motif consists of hhhhD(D/E), where h represents any hydrophobic amino acids. The Walker A motif is

responsible for binding nucleotides, and the Walker B motif coordinates Mg^{2+} ions and water molecules to catalyze the hydrolysis of nucleotides. Structural studies on classical members of AAA^+ ATPase including Cdc48, p97, ClpX, N-ethylmaleimide-sensitive-factor (NSF), and FtsK showed that AAA^+ proteins tend to form ring-like structures for function[14-22]. Similarly, earlier low-resolution electron microscopy showed that RuvB assembles into a hexamer on HJ DNA, forming a tripartite complex by flanking a RuvA octamer on both ends[23,24]. However, the low-resolution structure of RuvA-RuvB-HJ limits a mechanistic understanding of Holiday junction branch migration.

Here, we present cryo-EM structures of RuvB in complex with dsDNA with resolutions up to 2.9 Å, showing that RuvB forms a spiral staircase to facilitate the HJ migration. During our manuscript preparation, similar structures of *S. thermophilus* RuvB in complex with RuvA and DNA were published in *Nature*[11]. The asymmetric hexameric assembly of RuvB, around dsDNA, provides a mechanistic understanding of Holliday junction migration, in which ATP hydrolysis drives conformational changes of RuvB, leading to the pulling and revolving of DNA inside the central pore of RuvB by two nucleotides per step. Moreover, our structural analysis also revealed that ATP hydrolysis occurs at the top position of the spiral staircase most probably in a sequential manner. Additionally, the asymmetric assembly of RuvB also indicates an asymmetric engagement with RuvA and an association-and-detachment mechanism for the interactions between RuvA and RuvB during HJ branch migration. Together, we demonstrate that HJ migration includes a series of highly coordinated events, including nucleotide cycling, RuvB conformational changes that trigger DNA pulling and revolving, as well as the association and detachment of RuvA to RuvB.

RESULTS

Overall structures of the RuvB-DNA Complex

To gain a mechanistic understanding of Holliday junction branch migration, we expressed and purified *T. thermophilus* RuvA and RuvB from *E. coli*. Then, we incubated RuvA and RuvB with DNA substrates in the presence of 2 mM ATP**γ**S to assemble the HJ complex. We also incubated RuvB with DNA substrates and 2 mM ATP**γ**S to assemble RuvB-DNA

complex, which was further purified by gel filtration (Fig. S1A-B). Gel filtration showed that RuvB alone may form a monomer while the RuvB and DNA assemble into a large complex (Fig. S1A-B). The purified samples were applied to cryo-EM grids for screening and data collection using an FEI Titan Krios equipped with a K3 detector (Figure S1C). As we failed to generate useful datasets for our HJ complex containing RuvA/RuvB/DNA, we focused on elucidating the assembly of the RuvB-DNA complex. Data processing in cryoSPARC resulted in two maps with overall resolutions of 2.97 Å and 3.20 Å (Fig. 1A-B, Fig. S2, Fig. S3A-D, & Table S1). These high-resolution maps allowed us to build atomic models of the RuvB-DNA complexes, denoted as RuvB hexamer and RuvB dodecamer models (Fig.1C-D, Fig. S4, & Table S1), respectively. The RuvB dodecamer is formed by two RuvB hexamers in a head-to-head manner with approximate dimensions of 158 Å × 127 Å × 127 Å (Fig. 1A & 1C). The RuvB hexamer has approximate dimensions of 80 Å × 127 Å × 127 Å (Fig. 1B & 1C). RuvB assembles into a ring-like hexamer with dsDNA in the central pore that directly contacts four subunits (Fig. 1C-D). The RuvB hexamer model resembles RuvB hexamers from the dodecamer with minor differences. Notably, a feature **β**-hairpin in the NTD of RuvB is invisible in most protomers of RuvB hexamer but is well defined in all the protomers of RuvB dodecamer (Fig. 1E). Similar differences were also observed between our RuvB hexamer and *S. thermophilus* RuvB hexamer (Fig. 1F). In the RuvB dodecamer, we observed interactions mediated by the feature **β**-hairpins of RuvB (Fig. 1C), whereas this feature hairpin interacts with the C-terminal domain of RuvA in *S. thermophilus* RuvB. These interactions, which are absent in our *T. thermophilus* RuvB hexamer, may stabilize the conformations of the feature **β**-hairpin in our RuvB dodecamer and in *S. thermophilus* RuvB. Moreover, the overlaid structures of our RuvB dodecamer and *S. thermophilus* RuvB showed obvious conformational changes with respect to the feature **β**-hairpins of equivalent protomers of RuvB (Fig. 1G). Together, these structural comparisons suggest that the feature **β**-hairpin of RuvB is conformationally flexible, which may be critical for its unique interaction mode with RuvA in the Holliday junction complex (See section of asymmetric interactions with RuvA).

As the RuvB hexamer, in complex with DNA, is sufficient to reveal the mechanism of HJ branch migration, we will focus all further discussions on the RuvB hexamer model in our manuscript.

Assembly of the RuvB Hexamer

Six RuvB protomers assemble into an asymmetric ring-like hexamer with a 3-3.4 nm-wide central pore that accommodates duplex DNA (Fig. 1D & 2A). As reported before, each protomer of RuvB is composed of an N-terminal domain ($RuvB^N$), a middle domain ($RuvB^M$), and a C-terminal domain ($RuvB^C$) (Fig. 2B & S5). More strikingly, each protomer (A to F) in the RuvB hexamer adopted a different conformation (Fig. 2C). We aligned the $RuvB^N$ domains of B to F with that of the target protomer A. The relative orientations of $RuvB^C$, $RuvB^M$, and $RuvB^N$ display clear deviations between protomers (Fig. 2C). In contrast, the separated individual domains of RuvB from each protomer of RuvB hexamer aligned well (Fig. S6A-C). Together, these data suggest that rigid body motions occur among the three domains of individual RuvB protomer during the assembly of the RuvB-DNA complex.

Compared to the previously determined crystal structure of RuvB (PDB code: 1HQC), protomers A, B, C, and D in the RuvB hexamer display large conformational changes, in which the CTDs rotate away from the NTDs (Fig. 2D & S6D). In contrast, protomer E is almost identical to the crystal structure of RuvB while protomer F displays small conformational variations (Fig. 2D & S6D). Interestingly, protomers A, B, C, and D are involved in DNA binding while E and F are DNA-disengaged protomers, suggesting that DNA engagement may trigger conformation changes of RuvB protomers from a closed to a more open conformation (Fig. 2E). Thus, we propose that the assembly of RuvB-DNA complex may be a cooperative process involved in multiple sequential events, including RuvB-DNA binding, DNA engagement triggered RuvB conformational changes and the establishment of neighboring RuvB-RuvB interactions (Fig. 2E).

The conformational diversity between RuvB protomers not only generates the asymmetric RuvB ring but also results in large variations among protomer interfaces (Fig. 3A & S7A-F). The interface between protomers B and C and the interface between protomers B and A are most extensive with buried areas of 3860 $Å^2$ and 3721 $Å^2$, respectively; the interface between protomers D and E and protomers D and C are less extensive with buried areas of 2508 $Å^2$ and 2256 $Å^2$, respectively; the interface between protomers E and F and the interface between protomers A and F are least extensive with

buried areas of 1562 Å^2 and 1537 Å^2, respectively (Fig. 3A). Detailed examination of interfaces between neighboring RuvB protomers showed that all three domains of one protomer pack tightly with domains of its partner in the AB dimer and BC dimer, whereas the interactions mediated by domain N are either reduced or abolished in the CD dimer, DE dimer, EF dimer, and AF dimer (Fig. 3B-D & Fig. S7A-F). Despite these differences, all the interfaces between RuvB protomers are dominated by charge-charge interactions (Fig. 3B-D). For example, in the BC dimer, D277 (C) and R147 (B), D216 (C) and R34 (B), R215 (C) and E39 (B), R212 (C) and E39 (B), R205 (C) and E115 (B), and R7 (C) and D116 (B) all form salt bridges to glue the protomers B and C together (Fig. 3E).

DNA Binding by RuvB

Duplex DNA density is clearly defined for more than 20 bp, which traverses the central pore of RuvB hexamer from one end to the other (Fig. 4A-B). Among the six protomers of the RuvB hexamer, four protomers (A, B, C, and D) assemble into a 'spiral staircase' for coordinating dsDNA while the other two protomers (E and F) close the spiral staircase without interacting with DNA substrate (Fig. 4A-B). Notably, different from the Ftsk hexamer that only interacts with one strand of dsDNA[21], both strands of the DNA substrate interact with RuvB protomers A, B, C, and D (Fig. 4C & S8A). Specifically, three conserved arginine residues R297, R300, and R302 in the RuvB^C domain form a motif known as an arginine finger to interact with the negatively charged DNA backbone at the HJ core-distal end (Fig. 4C, S8A, & S5). Four arginine fingers from the DNA-interacting protomers were nicely positioned in a helical path to follow the DNA's helix precisely and established strong interactions with both strands of the duplex DNA substrate. Moreover, we observed a second DNA-engagement site in our structure, which was not seen in the *S. thermophilus* structure, perhaps due to poor DNA density at the corresponding site. R101 next to the Walker B motif and R104 in the **β**6-**β**7 loop, two highly conserved residues across species, engaged the backbone of one strand of the dsDNA (Fig. 4D, S8B, & S5). As all the DNA-engaging arginine residues interact with the phosphate backbone, RuvB can bind to any DNA substrates without sequence preference. Notably, we also noticed that in both DNA-engagement sites, the DNA-interacting arginine residues from protomers B and C are closer to the phosphate backbone than those from

protomers A and D, suggesting that protomers B and C engage with DNA more tightly than protomers A and D (Fig. S8A-B). This observation is consistent with the different functional roles of protomers A, B, C, and D during DNA translocation. In addition, the DNA-engaged arginine residues form a repeated binding pattern along one strand of dsDNA separated by the distance of two nucleotides (about 7 Å) (Fig. 4C-E), suggesting that the DNA substrate migrates about 7 Å at each step catalyzed by RuvB.

Nucleotide Cycling

Adenine nucleotides were observed to be located at the interface of two adjacent subunits and are exclusively nested in a cleft formed by domains $RuvB^N$ and $RuvB^M$ of one RuvB protomer in *cis* (Fig. 5A-B). Consistent with a previous observation in the crystal structure of RuvB, the adenine base lies in a hydrophobic cleft, which is composed of Y14, I15, Y168, and the side chain of R179 (Fig. 5A-B)[9]. The phosphate groups are coordinated by R7, R205, and the conserved Walker A motif, specifically K51 (Fig. 5A & S5). R158 from the adjacent subunit in *trans* also interacts with the nucleotide phosphate groups (Fig. 5A). A magnesium ion was observed to be in proximity to the γ-phosphate and was coordinated by the conserved Walker B motif residues D97 and E98. (Fig. 5A & S5). To our surprise, the six promoters of RuvB hexamer bind different adenine nucleotides (Fig. 5C). Promoters B, C, and D bind ATP molecules while protomers A, F, and E coordinate ADP molecules (Fig. 5C). Among the four DNA-engaging protomers, both protomers B and C contain ATP molecules based on the nicely fitted nucleotide density (Fig. S9A). Notably, protomer A, located at the top of the staircase, might contain either ADP or ATP with higher occupancy for ADP since ADP can be nicely fitted into the density with a sigma value of 1.8 while ATP can also be nicely placed into the density when we raised the sigma value to 2.5 (Fig. 5D). This observation suggested that ATP hydrolysis occurs at the top of the staircase between protomers A and F. After ATP hydrolysis, the ADP molecules remain associated with RuvB at positions F and E (Fig. S9B). The ADP to ATP exchange may occur at the position of protomer D as the nucleotide density in protomer D is very poor, likely due to low occupancy of nucleotides at this position (Fig. 5E). Thus, ATP hydrolysis and exchange are spatiotemporally separated in the asymmetric hexamer of RuvB. Furthermore, this observation also indicates that nucleotide exchange and ATP

hydrolysis are two discrete steps coordinated by the interfaces of protomers ED and AF, respectively.

To further understand why ATP hydrolysis occurs in protomer A but not others, we analyzed the interfaces of RuvB neighboring protomers. To our surprise, residues R158, E115, and D116 in a trans (adjacent) protomer, which are critical for ATP hydrolysis, are not positioned well for catalysis in the AF dimer but primed for catalysis in the CB dimer and the BA dimer (Fig. 5F-H & S9 C-D). Specifically, R158, which is involved in stabilizing the conformation of the **γ**-phosphate of ATP is far away from **γ**-phosphate in the AF dimer; E115 was supposed to but did not form a salt-bridge with R205 in the AF dimer; D116 also pointed away from the catalytic center in the AF dimer (Fig. 5F & 5G). These results suggested that the conformation of the AF dimer we captured may represent a post-hydrolysis state. In contrast, the conformations of the BA and the BC dimers represent a primed-catalysis state. This raised the question as to why ATP hydrolysis cannot occur at positions B and C. We speculate that the extensive interaction interfaces in the BA dimer and the BC dimer may limit conformational changes within the N domain, which is critical for ATP hydrolysis. Additionally, the tight interfaces may also limit the free access of water molecules to the catalytic centers of the BA and BC dimers. Consistent with this speculation is that we observed unmodelled densities in the catalytic center of the AF dimer (Fig. 5I), which may be contributed to water molecules. A similar observation was also made in the *S.thermophilus* structure, providing another piece of evidence in support of our speculation.

Asymmetric Interactions with RuvA

Previous studies have revealed that RuvB C-terminal domain interacts with RuvA with a stoichiometry of 6:4[8,11,25]. The asymmetric assembly of RuvB hexamer provides a rational explanation for the previously mentioned studies. To dissect which protomers in the RuvB hexamer can interact with RuvA, we docked the RuvA CTD to the RuvB NTD based on the crystal structure of the RuvB and RuvA CTD complex, which reveals that the feature **β**-hairpin in RuvB NTD is critical for the recruitment of RuvA CTD[8]. Protomers A, F, E, and D have sufficient space to establish interactions with RuvA (Fig. 6A). In contrast, protomers B and C cannot accommodate the CTD of RuvA due to clashing of residues

induced by steric hindrance with neighboring RuvB protomers (Fig. 6B-C). Therefore, the asymmetric assembly of the RuvB hexamer determines the 6:4 stoichiometry between RuvB and RuvA in the HJ complex. As RuvA can only engage with four protomers, we speculate that RuvA domain III undergoes cycles of transient dissociation from and reattachment to RuvB during HJ branch migration at the A, F, E, and D positions, similar to a carbon brush in an electric generator. Furthermore, the intrinsically disordered nature of the feature **β**-hairpin in RuvB may also facilitate the dynamic interactions between RuvA and RuvB.

Mechanisms of Holliday Junction Migration

Our structural analysis allowed us to propose a model for the HJ branch migration catalyzed by the asymmetric RuvB hexamer (Fig. 6D, Supplementary Movie 1). RuvB protomers are recruited by RuvA to the HJ and assemble into an asymmetric hexamer bound to ATP. The sequential cycling of ATP hydrolysis, ADP release, and ATP exchange triggers concerted conformational changes of RuvB protomers, leading to the revolution of RuvB around duplex DNA, accompanied by a pulling motion of DNA from the HJ core (Fig. 6D). HJ branch migration is advanced by two nucleotides at the cost of one ATP molecule for each step or 12 nucleotides at the cost of 6 ATP in one complete revolution of RuvB. Due to steric hindrance in positions B and C, RuvA undergoes cycles of dissociation and reattachment to RuvB protomers, which also prevents dsDNA from forming a knot, kinking, breaking, or building up excessive torsion during HJ migration.

DISCUSSION

In earlier studies, two models have been proposed to explain the molecular mechanisms of AAA^+ motor proteins: one being the rotation model and the other a revolution model[26]. In the rotation model, motor proteins rotate on their own axis, while revolution motor proteins revolve around their substrates, similar to a planet's day vs year cycle. Structurally, rotation motors tend to form oligomers with a small central pore (diameter < 2.0 nm) and revolution motors generally display a large central pore (diameter > 3.0 nm)[26]. All protein translocases with structures available for analysis, including Cdc48, p97, and Clpx, display a small pore and have five subunits engaged with their substrates[15-18]. Our

structure of RuvB hexamer clearly showed that RuvB forms a ring-like structure with a large central pore (3.4 nm), which has enough space for RuvB to revolve around the DNA duplex, and that RuvB has four protomers engaging DNA, contrasting those with small pores.

It may be a universal mechanism that AAA$^+$ ATPases tend to form asymmetric spiral staircases in the presence of substrates for function. Earlier AAA$^+$ ATPase studies revealed that most AAA$^+$ ATPases form symmetric oligomers[12,13,22,27-30]. At that time, most structures of AAA$^+$ ATPase were determined in the absence of substrates due to technical challenges in obtaining crystals of AAA$^+$ ATPases in complex with substrates. With the advancement of cryo-EM single particle analysis, more and more cryo-EM structures of AAA$^+$ ATPase in complex with substrates were published, revealing that a spiral assembly of AAA$^+$ ATPase hexameric rings is universally shared to facilitate the translocation of substrates through the pore. In our case, we also observed that RuvB assembles into a spiral staircase with dsDNA in the central pore. More interestingly, four protomers of RuvB hexamer engage with dsDNA, indicating a coupled mechanism of revolution and translocation by RuvB to facilitate Holliday junction migration.

Furthermore, ATP binding, ATP hydrolysis, and ADP release are key events driving the conformational changes of AAA$^+$ ATPases for triggering the “hand-over-hand” movement of the arginine finger pore loops that facilitate the unidirectional movement of substrates. At least three models have been proposed for mechanisms of ATP hydrolysis by AAA$^+$ ATPases, including a synchronized model, stochastic model, and sequential model[31-33]. Our structural study on RuvB, together with a previous structural study on *S. th* RuvB, came to a census that RuvB hydrolyzes ATP most probably in a sequential manner, in which ATP hydrolysis occurs at the uppermost position of the spiral staircase, while ATP is loaded at the lowest point of the spiral staircase. In the published manuscript on *S. thermophilus* RuvB, it was proposed that ADP release triggers ATP hydrolysis through a signaling mechanism across protomers of RuvB hexamer[11]. However, from our structural analysis of RuvB hexamer, we did not see strong evidence to support this cross-protomer communication. Instead, we tend to believe that ATP hydrolysis occurs at the top position of the spiral staircase mainly because the RuvB protomer at that point and its neighboring protomer in *trans* are better positioned for ATP hydrolysis than the other

subunits. In addition, the relatively poor density of ATPγS in the nucleotide-binding pocket of protomer D suggested that ATPγS may have relatively low occupancy. Some particles may have ADP or are empty at the position of protomer D. Considering that protomer E is occupied by ADP while protomer C has an ATP in its pocket, we posit that the exchange of ADP to ATP takes place at the position of protomer D, consistent with what was proposed in a recent publication[11].

Lastly, RuvB is loaded onto HJ DNA by interacting with RuvA, which assembles as a tetramer to bind to the HJ core. The asymmetry of RuvB's hexameric assembly provides a mechanistic explanation for the 6:4 stoichiometry between RuvB and RuvA, which is also supported by the complex structure of RuvA/RuvB/HJ published recently[11]. Domain III of RuvA, which is linked to the CTD RuvB winged helix DNA binding domain through a flexible linker, forms interactions with the feature beta-hairpin of RuvB, which is a conformationally flexible motif in RuvB. These features enable a mechanism of association and detachment between RuvA and RuvB during the revolution of RuvB, similar to the working mechanism of the carbon brush and the motor in an electric generator. Thus, the concerted events of nucleotide cycling, RuvB conformational oscillation, DNA pulling and rotating, as well as RuvA association and detachment ensure a precise branch migration of HJ by 2 nucleotides per step.

MATERIALS AND METHODS

Protein expression and purification

RuvB from *T. thermophilus* was cloned into pET-28a(+) expression vector with an N-terminal histidine tag, using the NdeI and SalI restriction sites. *Tt*RuvB was recombinantly expressed using RipL *E. coli* cells, BL21(DE3) strain. Bacterial cells were grown at 37 °C in LB supplemented with 50 μg mL^{-1} kanamycin until they reached an OD_{600} of about 0.6. Expression of RuvB was induced by the addition of 0.5 mM isopropyl β-D-1-thiogalactopyranoside (IPTG) and cultures were further incubated at 18 °C for 16 hours. Cells were pelleted at 4,000 rpm for 20 minutes at 4 °C, resuspended in 20 mM Tris-HCl pH 7.5, 300 mM NaCl lysis buffer, supplemented with cOmplete mini protease inhibitor cocktail (Roche), disrupted by sonication, incubated in a water bath at 55 °C for 30 min, and the resulting lysate was centrifuged at 18,000 rpm for 60 minutes at 4 °C. The supernatant was loaded onto a column containing Ni-NTA beads (Qiagen) that were pre-equilibrated with lysis buffer. The column was washed with 10 column volumes (Vc) of 20 mM Tris-HCl pH 7.5, 300 mM NaCl, 30 mM imidazole wash buffer, followed by elution of RuvB using 5 Vc of 20 mM Tris-HCl pH 7.5, 300 mM NaCl, 300 mM imidazole elution buffer, in 1 mL aliquots. Eluted protein was pooled, dialyzed against 20 mM Tris-HCl pH

7.5, 150 mM NaCl gel filtration buffer, and concentrated to 2 mL using an Amicon ®Ultra 30,000 NMWL centrifugal filter (Millipore), before application to a Superdex 200 10/300 GL Increased column (Cytvia) to purify protein to homogeneity. RuvB was eluted with gel filtration buffer on an ÄKTA go FPLC (Cytvia). RuvB presence was verified by SDS-Page gel, stained with Coomassie blue and protein concentration was determined by nanodrop A280 (35,973 MW, extinction coefficient 11,920).

DNA substrate and RuvB/DNA complex preparation

The HJ-DNA substrate was prepared by annealing the four following synthetic DNA oligonucleotides as described in [23]: HJ1 (AGAATCTGCCGAGAGACCGAGCAGAATTCTATGTGTTTACCAAGCGCTG), HJ2 (CAGCGCTTGGTAAACACATAGAATTCTGCTCGGTCTGAGCCGTCTAAGA), HJ3 (TCTTAGACGGCTCACTGGCTGTGGGATCCGAGCTGTCTAGAGACATCGA), HJ4 (TCGATGTCTCTAGACAGCTCGGATCCCACAGCCAGTCTCGGCAGATTCT). The four strands were mixed at equimolar ratios and were incubated at 95 °C for 10 minutes before allowing to cool to room temperature. The RuvB/DNA complex was reconstituted by mixing the purified RuvB with synthesized HJ-DNA at 1:6 (DNA/RuvB monomer ratio) in 20 mM Tris-HCl pH 7.5, 10 mM $MgCl_2$, 1 mM DTT, and 2 mM ATP-γ-S buffer for 30 min at 37 ºC. The complex was purified from monomeric RuvB via gel filtration using 20 mM Tris-HCl, 150 mM NaCl buffer. Complex purity was determined by SDS-Page gel and DNA presence was determined by agarose gel stained with ethidium bromide. Only the peak pertaining to RuvB/DNA complex was used in further testing.

Data Collection

Quantifoil 1.2/1.3, 300 mesh copper grids (Quantifoil) were glow discharged at 0.2 atm for 30 seconds and were loaded onto a FEI vitrobot (Thermo Fisher). 3uL of the sample was applied to the grid face before blotting for 4s and plunge freezing in liquid ethane. Grids were stored in liquid nitrogen prior to screening on a 200 kV Glacios (Thermo Fisher Scientific) equipped with a K3 bioquantum detector (Gatan, Inc.). Grids were again stored in liquid nitrogen until data could be collected using a 300 kV Titan Krios (Thermo Fisher Scientific), also equipped with a K3 detector. 6870 movies were collected, using data acquisition software EPU (Thermo Fisher Scientific), at a magnification of 81,000x and a pixel size of 1.08 Å, at a total dose of 50 $e^-/Å^2$. All data processing, including patch motion correction and contrast transfer function (CTF) calculations were performed in cryoSPARC (ver. 3.2)[34].

Structural Reconstruction and Model Building

Approximately 500 particles were manually picked from 65 exposures for initial 2D classification, creating six 2D classes that were used to train the template picker job. After manual inspection of template picker picks, 6874881 particles were picked from 6723 micrographs that showed clear features of target particles. Two rounds of 2D classification were performed to remove poor-quality particles. Multi-class ab-Initio reconstructions were performed using 884,750 particles and yielded four volumes for subsequent 3D classification ranging from 3.51-6.59 Å, estimated by the “gold standard” Fourier shell correlation of 0.143 [35]. Heterogenous refinement of an Ab-initio volume

containing 305,449 particles followed by non-uniform refinement produced a final volume at 3.2 Å, using C2 symmetry. Additionally, a mask was generated over a map volume pertaining to a single hexamer of the 3.2 Å map in UCSF Chimera (ver. 1.15), which was used in conjunction with local refinement of a heterogeneously refined volume containing 390,143 particles to yield a final volume at 2.97 Å using C1 symmetry. The two final volume maps were used for model building, post-processing, and interpretation using Phenix (ver. 1.20.1), UCSF Chimera (ver. 1.15), coot (ver. 0.9.8.1), and PyMol (ver. 2.1)[36-38].

ACKNOWLEDGEMENTS

We thank Xiaoyuan Yang for her assistance in making figures. Grid screenings were performed at OSU CEMAS with the assistance of Drs. Giovanna Grandinetti and Yoshie Narui. Cryo-EM data were collected with the assistance of Drs. Adam D. Wier, Thomas J. Edwards, Tara Fox, and Jenny Wang at the National Cancer Institute Cryo-Electron Microscopy Center supported by grants from the NIH National Institute of General Medical Sciences (GM103310). Anthony D. Rish is supported by an NIH T32 (GM118291-05 and GM144293-01).

Author Contributions

T.M.F. conceived the project. A.D.R., C.Z., and T.M.F. performed molecular cloning of and biochemical purification of RuvA and RuvB, and the biochemical reconstitution of the RuvB-DNA complex. Z.S., T.M.F, and A.D.R. prepared grids, determined the cryo-EM structures, and built the models. T.M.F., A.D.R., and Z.S. analyzed the data. T.M.F. and A.D.R. wrote the manuscript with inputs from all the authors.

CONFLICT OF INTEREST

All authors declare they have no conflict of interest.

DATA AVAILABILITY

Accession numbers for RuvB dodecamer and RuvB hexamer are as follows: (coordinates of atomic models: 8EFY and 8EFV, deposited to Protein Data Bank), and (density map: EMD-28107 and EMD-28101, deposited to Electron Microscopy Data Bank). All data needed to evaluate the conclusions in the paper are present in the paper.

REFERENCES

1 Tiwari, V. & Wilson, D. M. DNA Damage and Associated DNA Repair Defects in Disease and Premature Aging. *The American Journal of Human Genetics* **105**, 237-257 (2019). https://doi.org:10.1016/j.ajhg.2019.06.005

2 Sharples, G. J., Ingleston, S. M. & Lloyd, R. G. Holliday junction processing in bacteria: insights from the evolutionary conservation of RuvABC, RecG, and RusA. *Journal of bacteriology* **181**, 5543-5550 (1999).

3 Stephen, C. W. The RuvABC proteins and Holliday junction processing in Escherichia coli. *Journal of Bacteriology* **178**, 1237-1241 (1996).

4 Hideo Shinagawa and Hiroshi, I. Processing the holliday junction in homologous recombination. *Trends in biochemical sciences* **21**, 107-111 (1996). https://doi.org:https://doi.org/10.1016/S0968-0004(96)10014-1

5 Molecular Genetics of Recombination. *Topics in Current Genetics* (2007). https://doi.org:10.1007/978-3-540-71021-9

6 Constantinou, A., Davies, A. A. & West, S. C. Branch Migration and Holliday Junction Resolution Catalyzed by Activities from Mammalian Cells. *Cell* **104**, 259-268 (2001). https://doi.org:10.1016/s0092-8674(01)00210-0

7 Roe, S. M. *et al.* Crystal Structure of an Octameric RuvA–Holliday Junction Complex. *Molecular Cell* **2**, 361-372 (1998). https://doi.org:10.1016/s1097-2765(00)80280-4

8 Yamada, K. *et al.* Crystal Structure of the RuvA-RuvB Complex. *Molecular Cell* **10**, 671-681 (2002). https://doi.org:10.1016/s1097-2765(02)00641-x

9 Yamada, K. *et al.* Crystal structure of the Holliday junction migration motor protein RuvB from Thermus thermophilus HB8. *Proceedings of the National Academy of Sciences* **98**, 1442-1447 (2001).

10 Putnam, C. D. *et al.* Structure and mechanism of the RuvB Holliday junction branch migration motor. *Journal of molecular biology* **311**, 297-310 (2001).

11 Wald, J. *et al.* Mechanism of AAA+ ATPase-mediated RuvAB–Holliday junction branch migration. *Nature* (2022). https://doi.org:https://doi.org/10.1038/s41586-022-05121-1

12 Neuwald, A. F., Aravind, L., Spouge, J. L. & Koonin, E. V. AAA⁺: A Class of Chaperone-Like ATPases Associated with the Assembly, Operation, and Disassembly of Protein Complexes. *Genome Research* **9**, 27-43 (1999). https://doi.org:10.1101/gr.9.1.27

13 Khan, Y. A., White, K. I. & Brunger, A. T. The AAA+ superfamily: a review of the structural and mechanistic principles of these molecular machines. *Critical reviews in biochemistry and molecular biology* **57**, 156-187 (2022).

14 Twomey, E. C. *et al.* Substrate processing by the Cdc48 ATPase complex is initiated by ubiquitin unfolding. *Science* **365**, eaax1033 (2019). https://doi.org:10.1126/science.aax1033

15 Cooney, I. *et al.* Structure of the Cdc48 segregase in the act of unfolding an authentic substrate. *Science* **365**, 502-505 (2019). https://doi.org:10.1126/science.aax0486

16 Pan, M. *et al.* Mechanistic insight into substrate processing and allosteric inhibition of human p97. *Nature Structural & Molecular Biology* **28**, 614-625 (2021). https://doi.org:10.1038/s41594-021-00617-2

17 Fei, X., Bell, T. A., Barkow, S. R., Baker, T. A. & Sauer, R. T. Structural basis of ClpXP recognition and unfolding of ssrA-tagged substrates. *eLife* **9** (2020). https://doi.org:10.7554/elife.61496

18 Fei, X. *et al.* Structures of the ATP-fueled ClpXP proteolytic machine bound to protein substrate. *eLife* **9** (2020). https://doi.org:10.7554/elife.52774

19 Ripstein, Z. A., Vahidi, S., Houry, W. A., Rubinstein, J. L. & Kay, L. E. A processive rotary mechanism couples substrate unfolding and proteolysis in the ClpXP degradation machinery. *eLife* **9** (2020). https://doi.org:10.7554/elife.52158

20 White, K. I., Zhao, M., Choi, U. B., Pfuetzner, R. A. & Brunger, A. T. Structural principles of SNARE complex recognition by the AAA+ protein NSF. *eLife* **7** (2018). https://doi.org:10.7554/elife.38888

21 Jean, N. L., Rutherford, T. J. & Löwe, J. FtsK in motion reveals its mechanism for double-stranded DNA translocation. *Proceedings of the National Academy of Sciences* **117**, 14202-14208 (2020). https://doi.org:10.1073/pnas.2001324117

22 Puchades, C., Sandate, C. R. & Lander, G. C. The molecular principles governing the activity and functional diversity of AAA+ proteins. *Nature Reviews Molecular Cell Biology* **21**, 43-58 (2020). https://doi.org:10.1038/s41580-019-0183-6

23 Kouta Mayanagi and Yoshie Fujiwara and Tomoko Miyata and Kosuke, M. Electron microscopic single particle analysis of a tetrameric RuvA/RuvB/Holliday junction DNA complex. *Biochemical and biophysical research communications* **365**, 273-278 (2008). https://doi.org:https://doi.org/10.1016/j.bbrc.2007.10.165

24 Miyata, T. *et al.* Two different oligomeric states of the RuvB branch migration motor protein as revealed by electron microscopy. *Journal of structural biology* **131**, 83-89 (2000).

25 Iwasaki, H. *et al.* Mutational analysis of the functional motifs of RuvB, an AAA+ class helicase and motor protein for Holliday junction branch migration. *Molecular Microbiology* **36**, 528-538 (2002). https://doi.org:10.1046/j.1365-2958.2000.01842.x

26 Guo, P., Noji, H., Yengo, C. M., Zhao, Z. & Grainge, I. Biological Nanomotors with a Revolution, Linear, or Rotation Motion Mechanism. *Microbiology and Molecular Biology Reviews* **80**, 161-186 (2016). https://doi.org:10.1128/mmbr.00056-15

27 Hanson, P. I. & Whiteheart, S. W. AAA+ proteins: have engine, will work. *Nature Reviews Molecular Cell Biology* **6**, 519-529 (2005). https://doi.org:10.1038/nrm1684

28 Gates, S. N. & Martin, A. Stairway to translocation: AAA+ motor structures reveal the mechanisms of ATP-dependent substrate translocation. *Protein Science* **29**, 407-419 (2020). https://doi.org:10.1002/pro.3743

29 Ogura, T. & Wilkinson, A. J. AAA⁺superfamily ATPases: common structure-diverse function. *Genes to Cells* **6**, 575-597 (2001). https://doi.org:10.1046/j.1365-2443.2001.00447.x

30 White, S. R. & Lauring, B. AAA+ ATPases: Achieving Diversity of Function with Conserved Machinery. *Traffic* **8**, 1657-1667 (2007). https://doi.org:10.1111/j.1600-0854.2007.00642.x

31 Martin, A., Baker, T. A. & Sauer, R. T. Rebuilt AAA + motors reveal operating principles for ATP-fuelled machines. *Nature* **437**, 1115-1120 (2005). https://doi.org:10.1038/nature04031

32 Lyubimov, A. Y., Strycharska, M. & Berger, J. M. The nuts and bolts of ring-translocase structure and mechanism. *Current Opinion in Structural Biology* **21**, 240-248 (2011). https://doi.org:10.1016/j.sbi.2011.01.002

33 Joly, N. & Buck, M. Engineered Interfaces of an AAA+ ATPase Reveal a New Nucleotide-dependent Coordination Mechanism. *Journal of Biological Chemistry* **285**, 15178-15186 (2010). https://doi.org:10.1074/jbc.m110.103150

34 Punjani, A., Rubinstein, J. L., Fleet, D. J. & Brubaker, M. A. cryoSPARC: algorithms for rapid unsupervised cryo-EM structure determination. *Nature Methods* **14**, 290-296 (2017). https://doi.org:10.1038/nmeth.4169

35 Scheres, S. H. W. & Chen, S. Prevention of overfitting in cryo-EM structure determination. *Nature Methods* **9**, 853-854 (2012). https://doi.org:10.1038/nmeth.2115

36 Afonine, P. V. *et al.* Towards automated crystallographic structure refinement with phenix.refine. *Acta Crystallographica Section D Biological Crystallography* **68**, 352-367 (2012). https://doi.org:10.1107/s0907444912001308

37 Pettersen, E. F. *et al.* UCSF Chimera?A visualization system for exploratory research and analysis. *Journal of Computational Chemistry* **25**, 1605-1612 (2004). https://doi.org:10.1002/jcc.20084

38 Emsley, P., Lohkamp, B., Scott, W. G. & Cowtan, K. Features and development of Coot. *Acta Crystallographica Section D: Biological Crystallography* **66**, 486-501 (2010).

FIGURES AND FIGURES LEGENDS

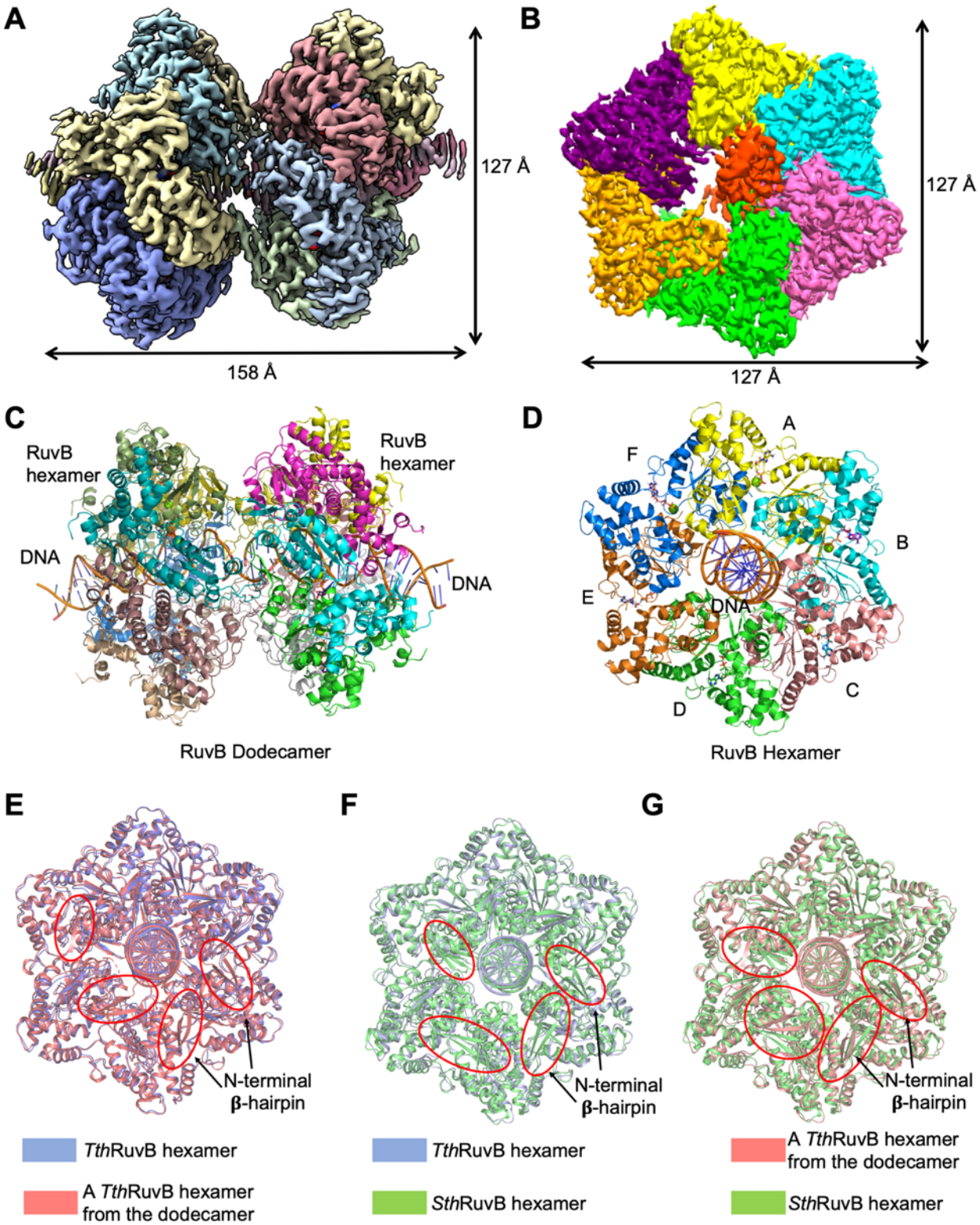

Fig. 1 Overall Structures of the RuvB-DNA Complex.

(A) The cryo-EM density map of RuvB dodecamer in complex with dsDNA with each subunit colored individually. The dodecamer has estimated dimensions of 158 Å by 127 Å by 127 Å.

(B) The cryo-EM density map of RuvB hexamer in complex with dsDNA with each subunit colored individually. The hexamer has estimated dimensions of 80 Å by 127 Å by 127 Å.
(C) Ribbon diagrams of RuvB dodecamer with dsDNA in the central pore.
(D) Ribbon diagrams of RuvB hexamer with dsDNA in the central pore with protomers A (yellow), B (cyan), C (salmon), D (green), E (orange), F (blue) colored differently. Nucleotides shown as sticks.
(D, F, G) Structural comparisons of *T. thermophilus* RuvB hexamer (blue), *S. thermophilus* hexamer (green, PDB 7PIS), and a *T. thermophilus* hexamer from the dodecamer (pink), revealing the conformational dynamics of a feature **β**-hairpin in the N-terminal domain of RuvB.

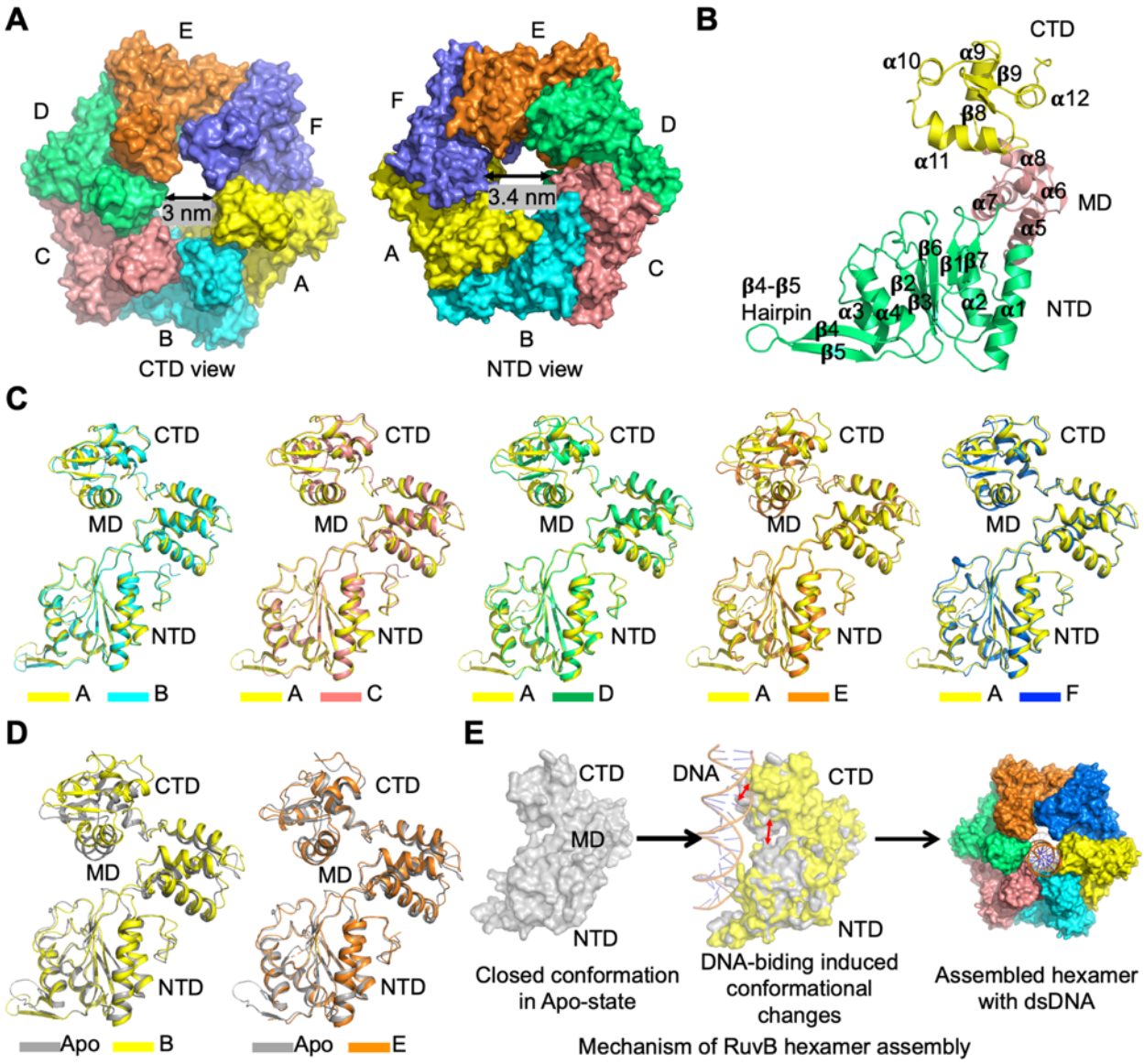

Fig. 2 The Assembly of RuvB Hexamer.

(A) Surface representation of RuvB hexamer with each protomer colored individually, showing the diameters of its central pore.

(B) Ribbon diagram of a RuvB protomer with secondary structural elements labeled.

(C) Overlaid structures of RuvB protomers with A in yellow, B in cyan, C in salmon, D in green, E in orange, and F in blue, revealing the conformational differences of the six protomers in RuvB hexamer.

(D) Structural comparisons of RuvB protomers B (yellow), E (orange), and the crystal structure of RuvB (grey).

(E) Diagrams illustrating a potential assembly mechanism of RuvB hexamer in complex with dsDNA.

A

Interface	Interface area (Å^2)
B/C	3860
B/A	3721
D/E	2508
D/C	2256
E/F	1562
A/F	1537

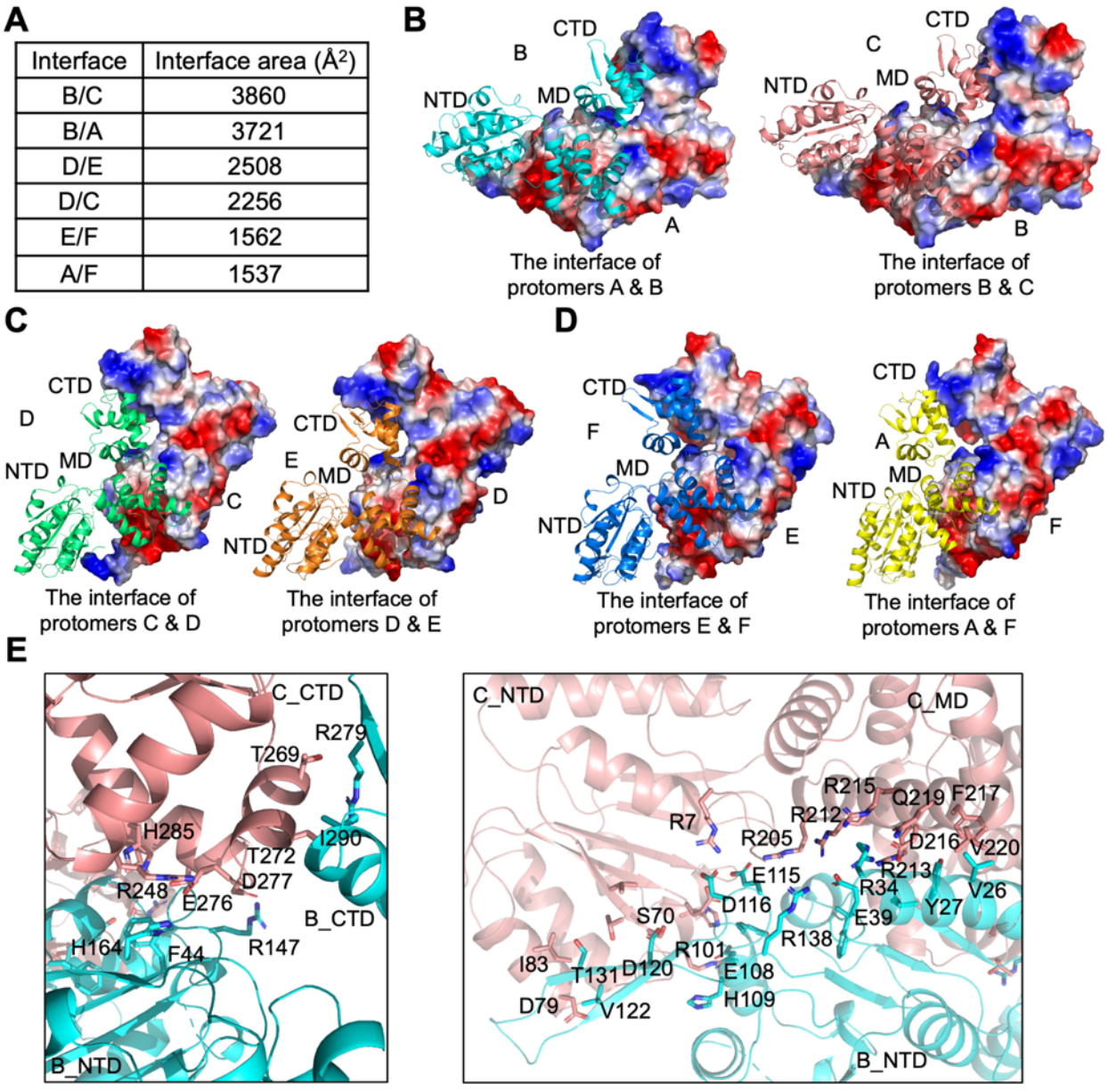

Fig. 3 Interfaces of RuvB Dimers.

(A) Buried interface areas of the six dimers in RuvB hexamer.

(B) The interfaces of the AB dimer and the BC dimer with electrostatic surface representation of protomers A and B and ribbon diagrams of protomers B (cyan) and C (salmon), respectively.

(C) The interfaces of the CD dimer and the DE dimer with electrostatic surface representation of protomers C and D and ribbon diagrams of protomers D (green) and E (orange), respectively.

(D) The interfaces of the EF dimer and the AF dimer with electrostatic surface representation of protomers E and F and ribbon diagrams of protomers F (blue) and A (yellow), respectively.

(E) Detailed interaction between protomers C and B with interface residues highlighted as sticks.

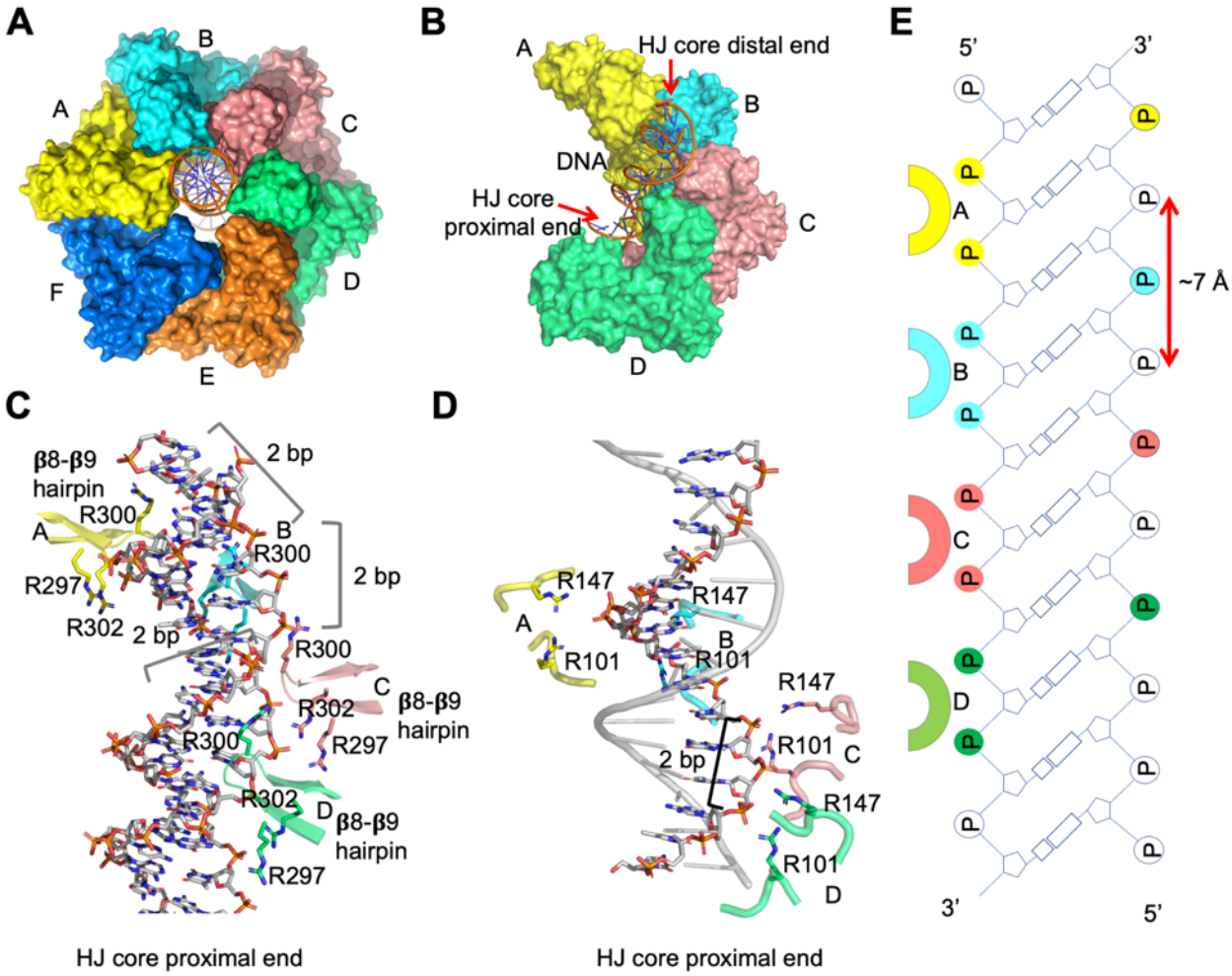

Fig. 4 DNA Engagement by RuvB

(A) Surface representation of RuvB-DNA complex with dsDNA highlighted as orange sticks.

(B) DNA in complex with the four DNA-engaging RuvB protomers, revealing an architecture of a spiral staircase by protomers A (yellow), B (cyan), C (salmon), and D (green).

(C) Ribbon diagrams showing interactions between dsDNA and the β8-β9 hairpin (Arginine finger) in the four DNA-engaging subunits. From one subunit to another, a RuvB protomer rotates about 60 degrees and rises 2 bp per revolution step following along the DNA helix.

(D) Ribbon diagrams showing interactions between dsDNA and Arg101 and Arg147 in the four DNA-engaging subunits.

(E) Schematic of the interface between the dsDNA substrate and the four staircase RuvB protomers.

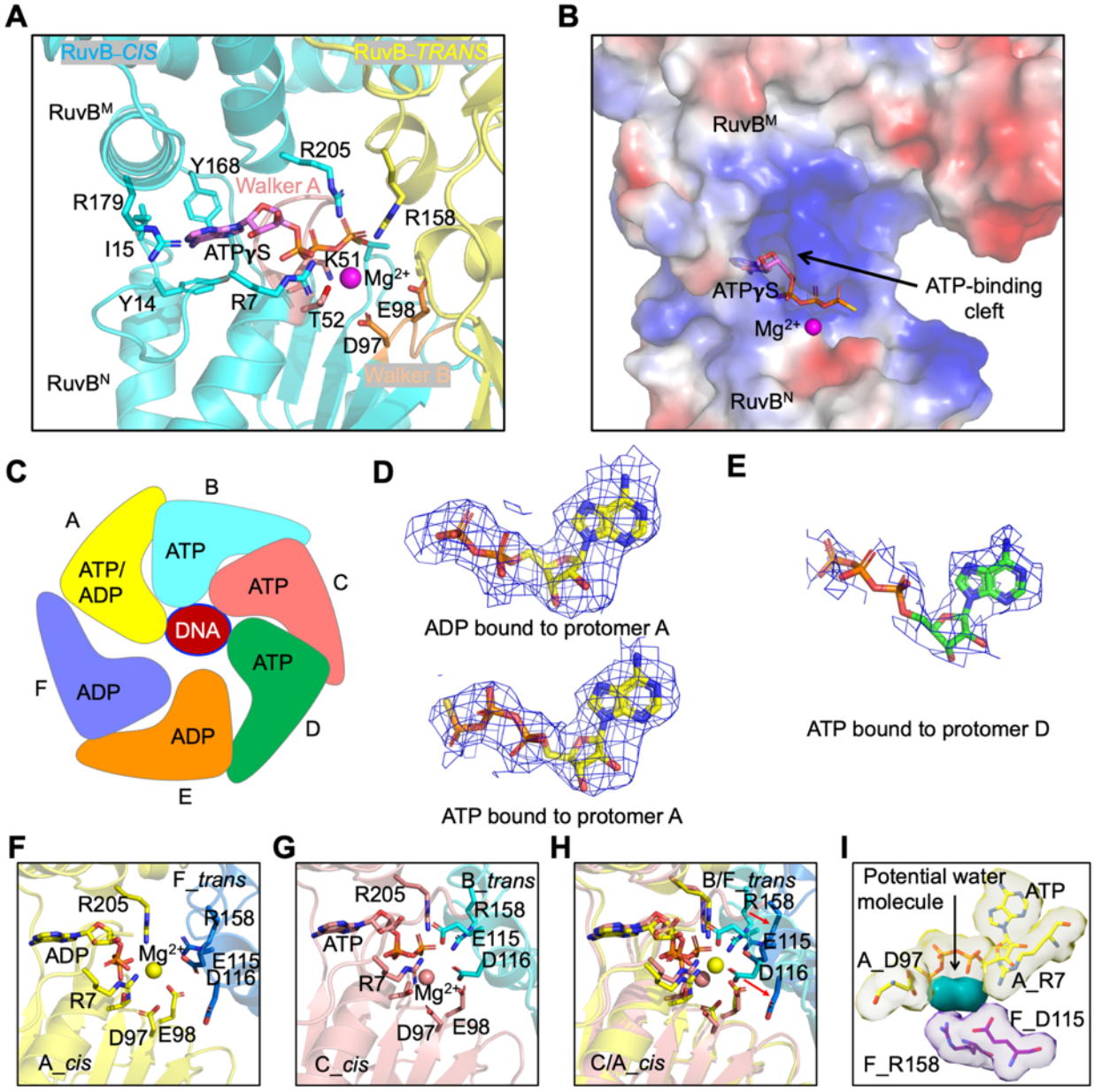

Figure 5 Nucleotide Binding Sites in RuvB Hexamer.

(A) ATP binding site in a representative RuvB dimer. ATP is coordinated by two protomers of RuvB (*cis* in blue and *trans* in yellow). ATP and residues responsible for coordinating ATP are highlighted in sticks. The magnesium ion for catalysis was highlighted as a sphere (pink). Walker A motif and Walker B motif were colored in salmon and orange, respectively.

(B) Electrostatic surface representation of the RuvB *Cis* subunit showing the binding pocket of ATP.

(C) Diagram illustrating the bound nucleotides in the six protomers of RuvB hexamer.

(D) ADP or ATP fitted to the cryo-EM density maps in protomer A at 2.5 **σ** or 2.0 **σ**, respectively.

(E) ATP fitted to the cryo-EM density maps in protomer D at 1.8 **σ**.

(F) The ATP catalytic center in the AF dimer with key residues for catalysis highlighted as sticks. Protomers A and F are shown in yellow and blue, respectively.
(G) The ATP catalytic center in the CB dimer with key residues for catalysis highlighted as sticks. Protomers C and B are shown in salmon and cyan, respectively.
(H) A comparison of the ATP catalytic centers in the AF dimer and the CB dimer reveals dramatic conformational changes in the trans protomers.
(I) Cryo-EM density maps (2.0 $\boldsymbol{\sigma}$) of the ATP catalytic center in the AF dimer, showing the unmodelled density (green) as potential water molecules.

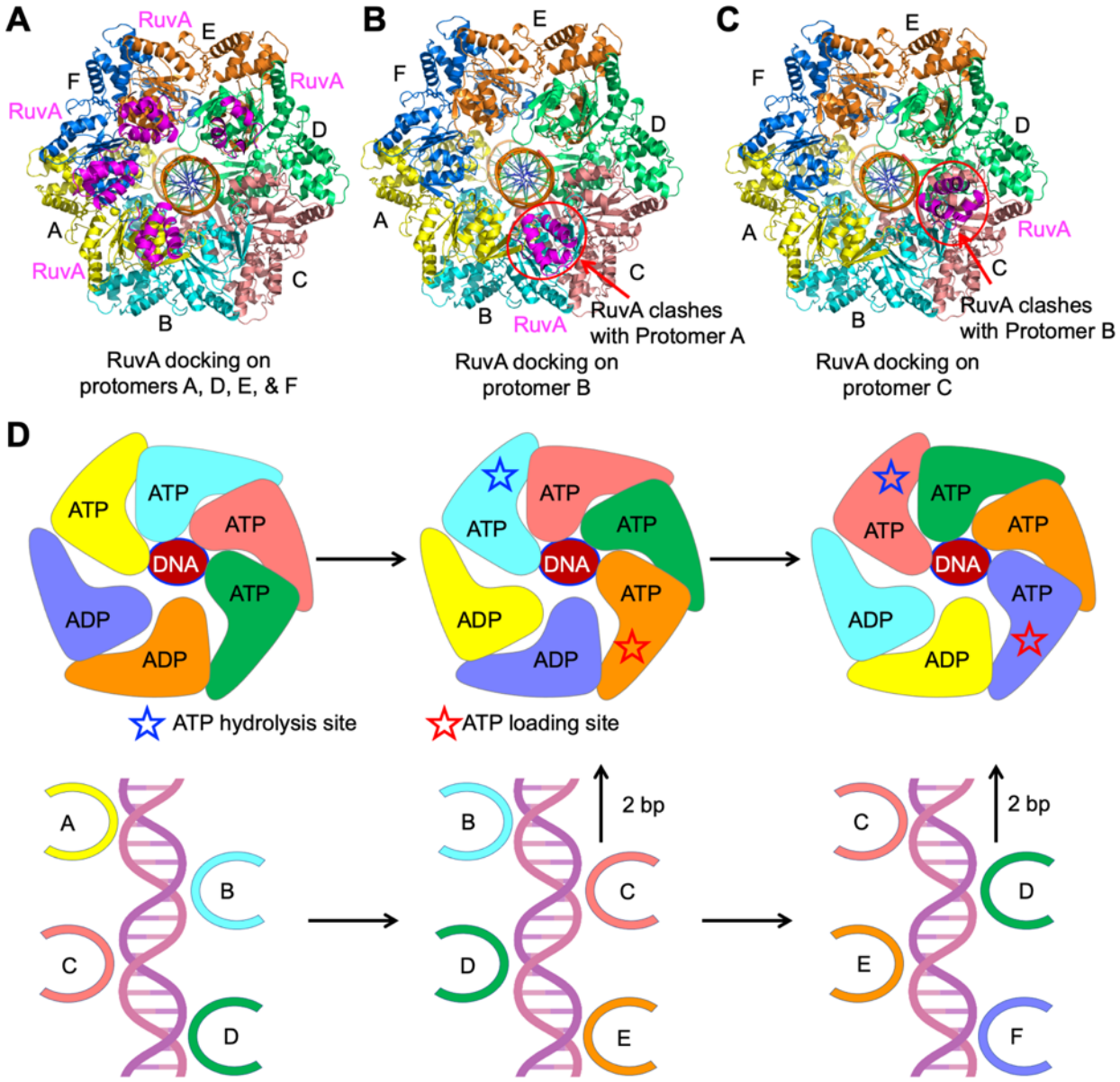

Figure 6. Mechanisms of RuvA Engagement and Holliday Junction Migration.
(A). Ribbon diagram showing the interactions between RuvA (magenta) and RuvB protomers A (yellow), D (green), E (orange), and F (blue).
(B). Ribbon diagram showing the interactions between RuvA (magenta) and RuvB protomer B (cyan), revealing that RuvA at position B can clash with protomer A.
(C). Ribbon diagram showing the interactions between RuvA (magenta) and RuvB protomer C (salmon), revealing that RuvA at position C can clash with protomer B.
(D). Diagram illustrating a mechanism of Holliday junction migration. RuvB and DNA assemble into a spiral staircase with four protomers engaged with DNA substrate. The ATP was hydrolyzed in a sequential manner and occurred one at a time at position A. At position D, ADP was exchanged for ATP. ATP hydrolysis drives the conformational changes of RuvB accompanied by revolving around and pulling of dsDNA by two base pairs at a time.

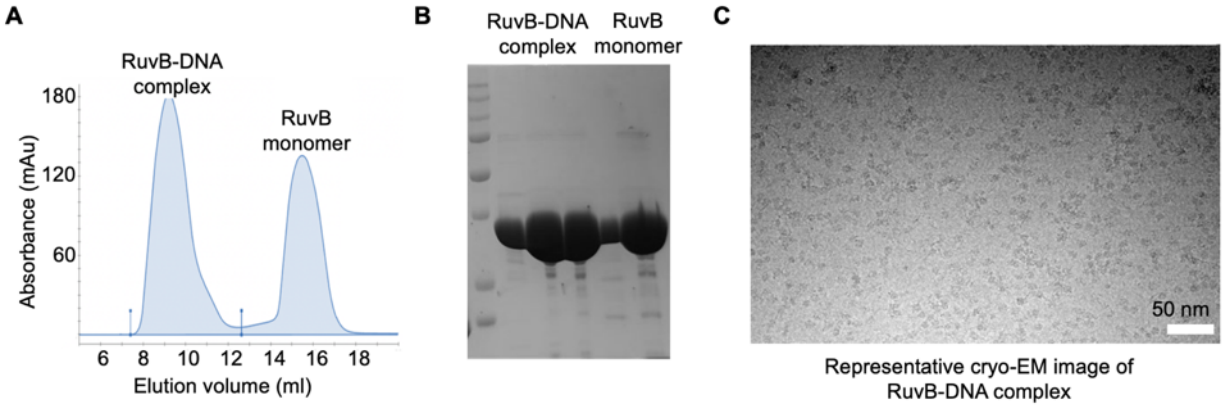

Fig. S1 Purification and Imaging of the RuvB-DNA complex.

(A) Gel filtration profile of the RuvB-DNA complex on a Superdex S200 10/300 GL Increased column.

(B) SDS-PAGE analysis showing the purified RuvB-DNA complex.

(C) A representative cryo-EM image of the RuvB-DNA complex.

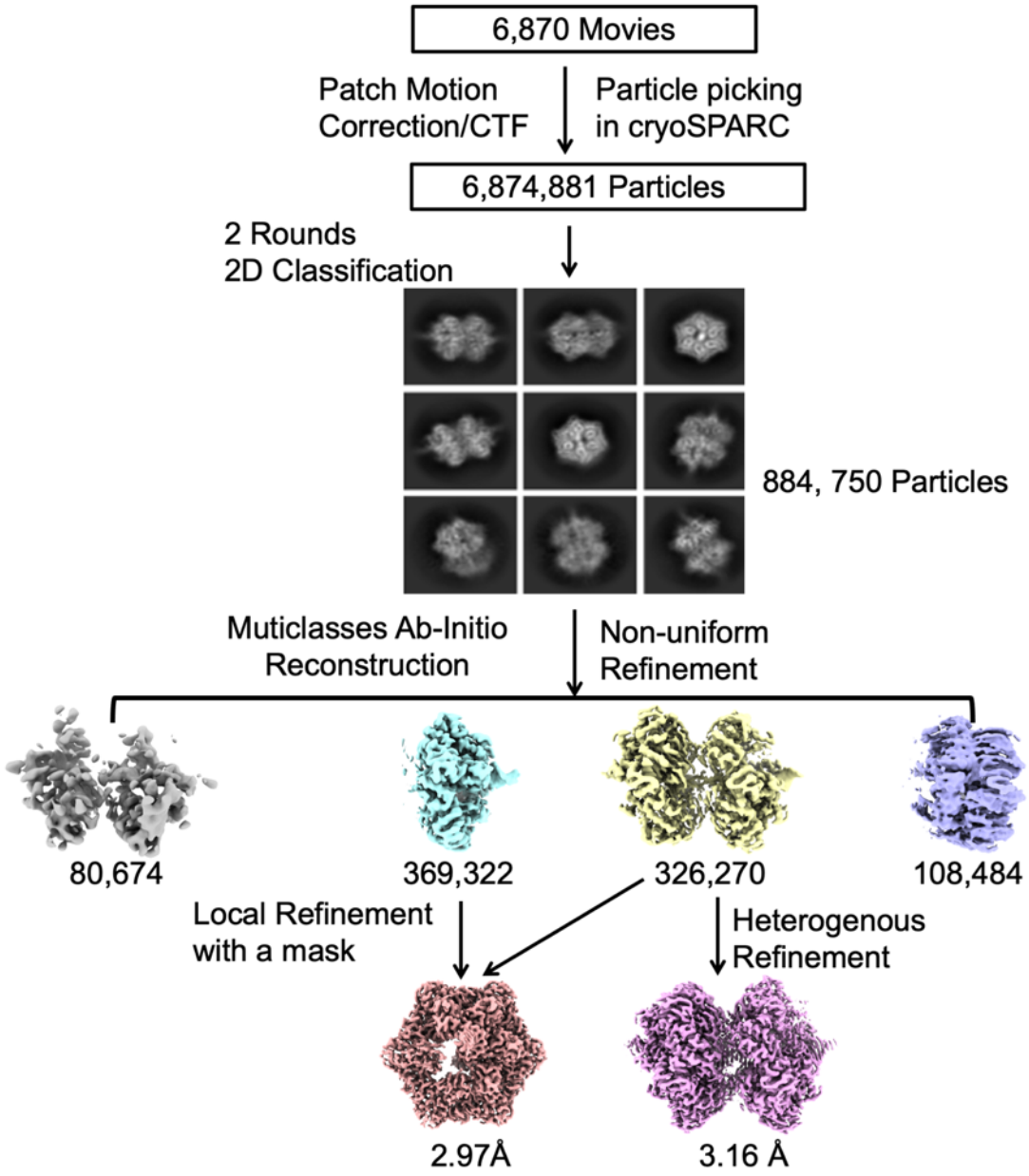

Fig. S2 Workflow of the RuvB-DNA complex 3D reconstruction using cryoSPARC.

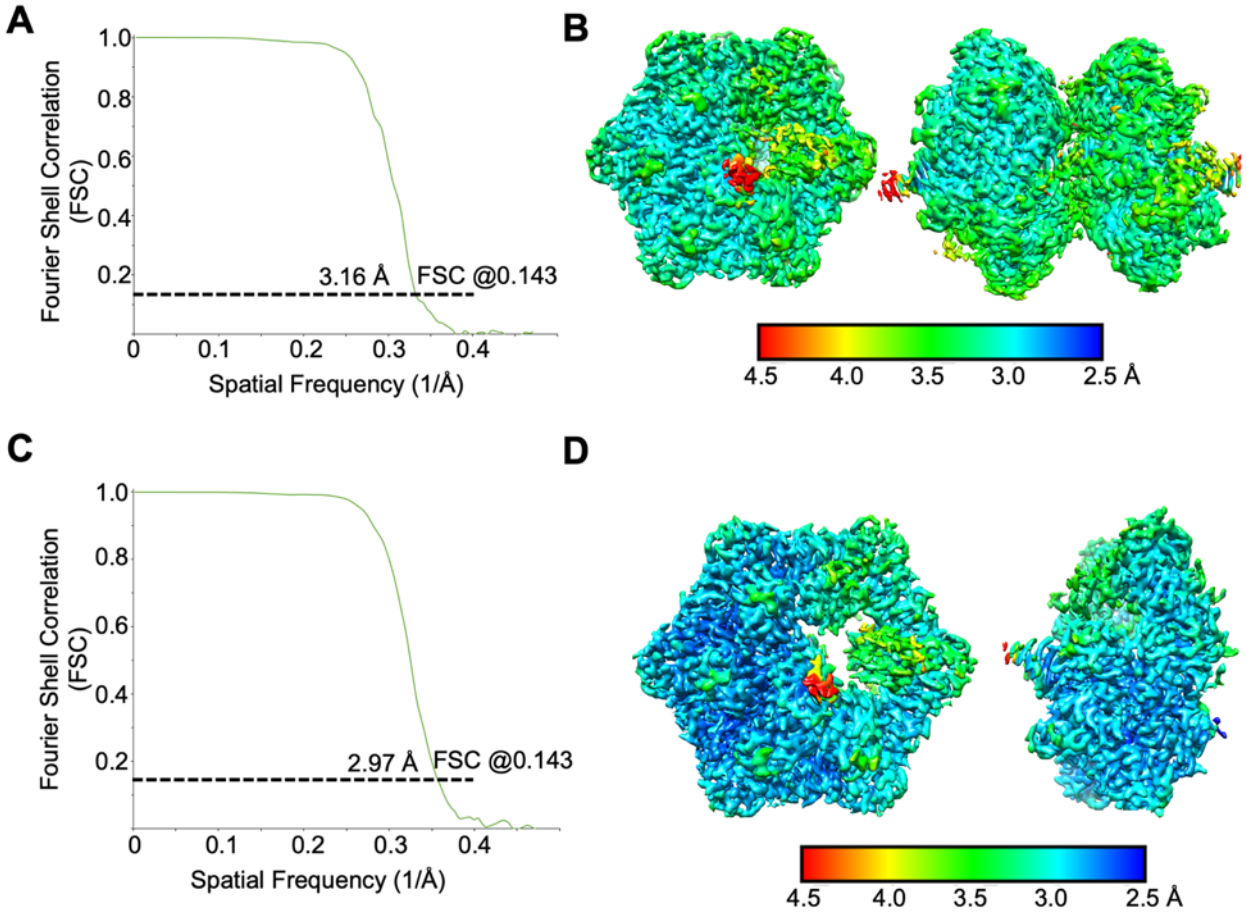

Fig. S3 Resolutions of the RuvB-DNA complexes.
(A) Fourier shell correlation (FSC) curve of 3D reconstructed RuvB dodecamer.
(B) Local resolutions of the RuvB dodecamer. Resolutions are color-coded by scale bars.
(C) Fourier shell correlation (FSC) curve of 3D reconstructed RuvB hexamer.
(D) Local resolutions of the RuvB hexamer. Resolutions are color-coded by scale bars.

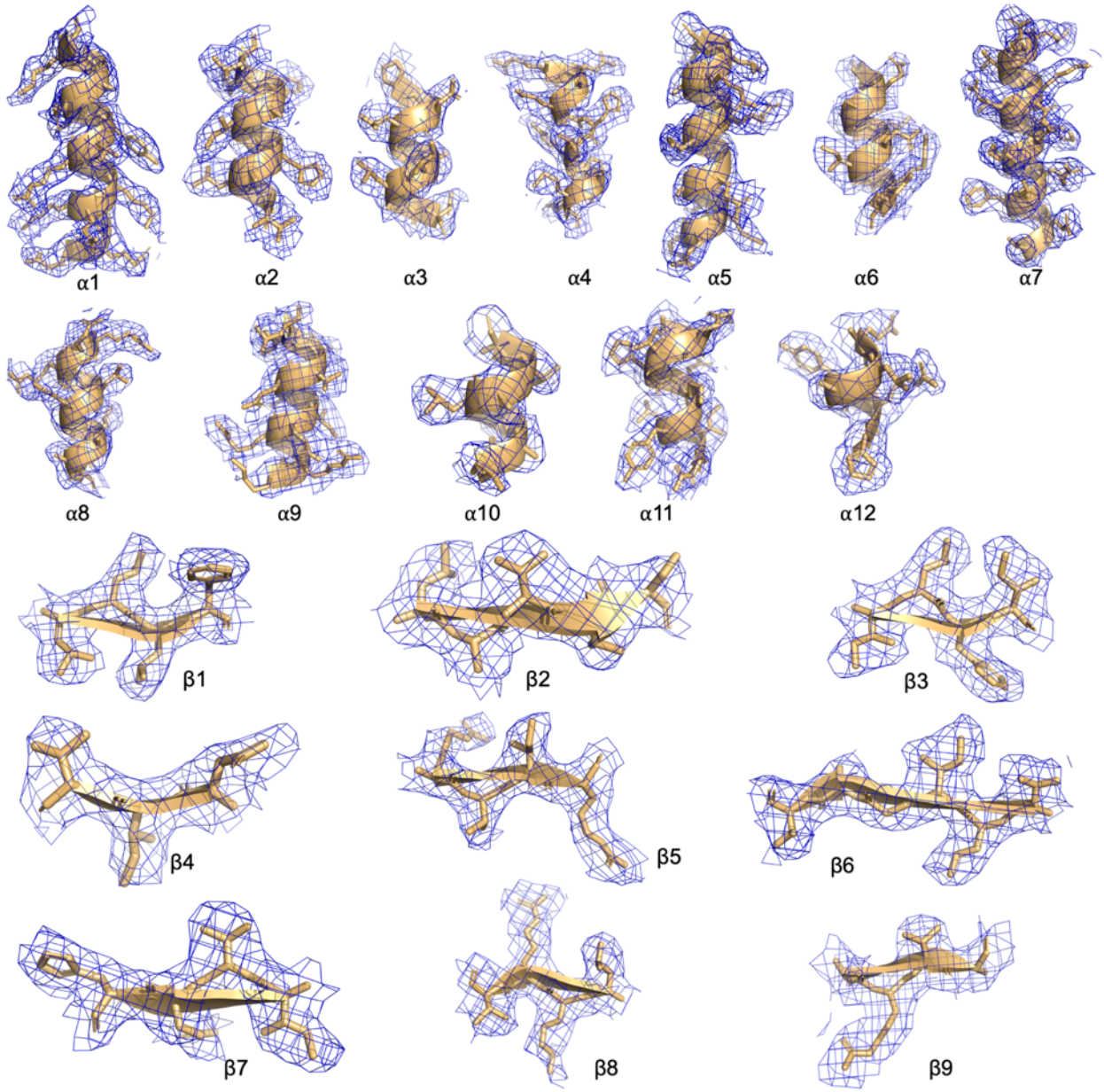

Figure S4 Cryo-EM Density of RuvB.
Representative segments of RuvB cryo-EM density map with the final atomic model (2.0 **σ**).

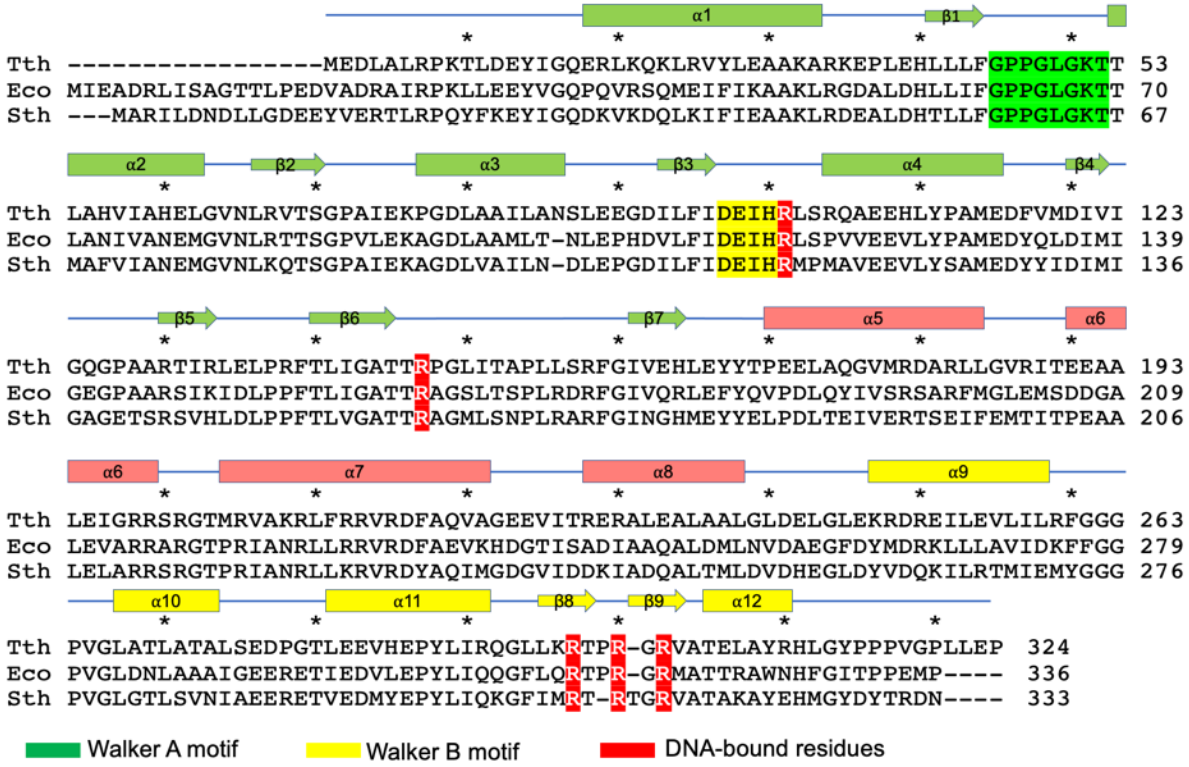

Fig. S5 Sequence Alignment of RuvB from Different Species.
Sequence alignment of RuvB from *Thermus thermophilus* HB8 (Tth), *Escherichia coli* K12 (Eco), and *Streptococcus thermophilus* (Sth) with secondary structural elements labeled above. NTD was highlighted in green, MD in salmon, and CTD in yellow. Walker A motif, Walker B motif, and arginine residues critical for coordinating DNA were highlighted in green, yellow, and red, respectively.

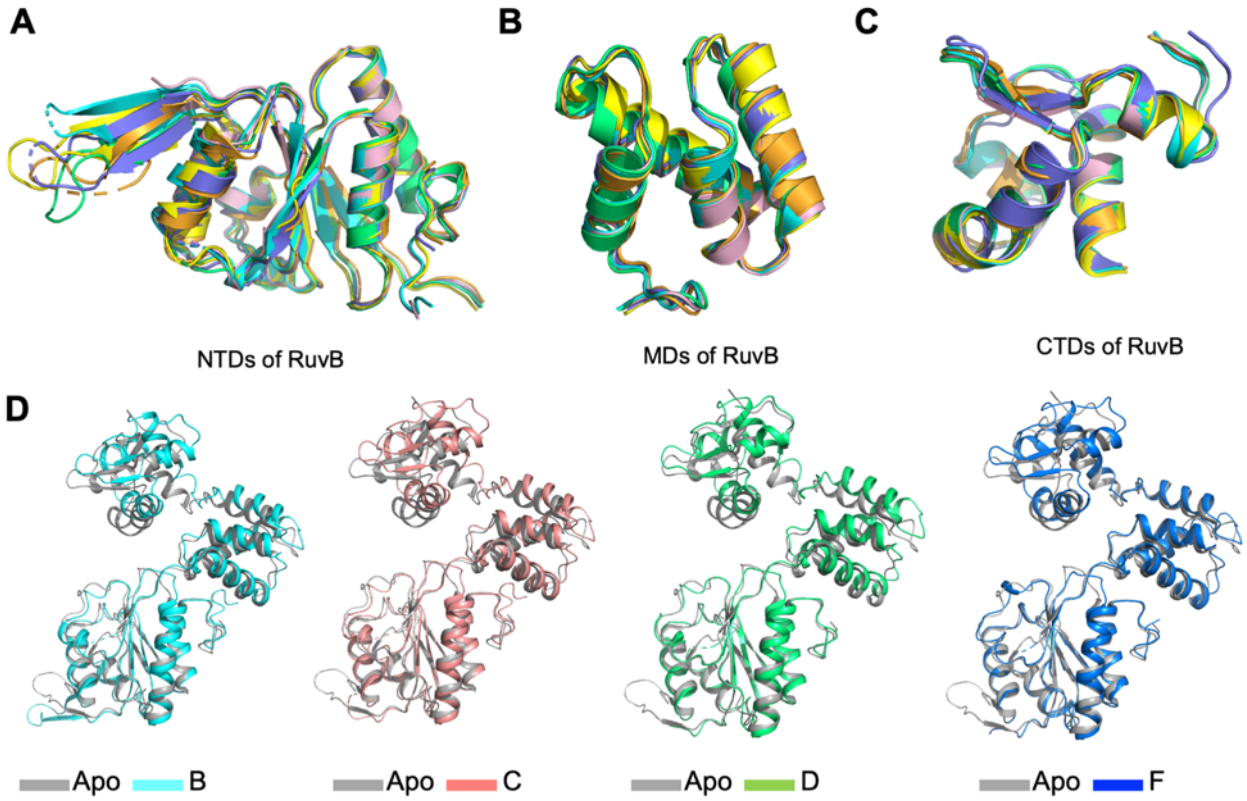

Fig. S6 Structural Comparison.
(A) Overlaid structures of RuvB N-terminal domains from the six RuvB protomers.
(B) Overlaid structures of RuvB middle domains from the six RuvB protomers.
(C) Overlaid structures of RuvB C-terminal domains from the six RuvB protomers.
(D) Structural comparisons of RuvB protomers B (cyan), C (salmon), D (green), F (blue) with the crystal structure of RuvB (1HQC) (grey).

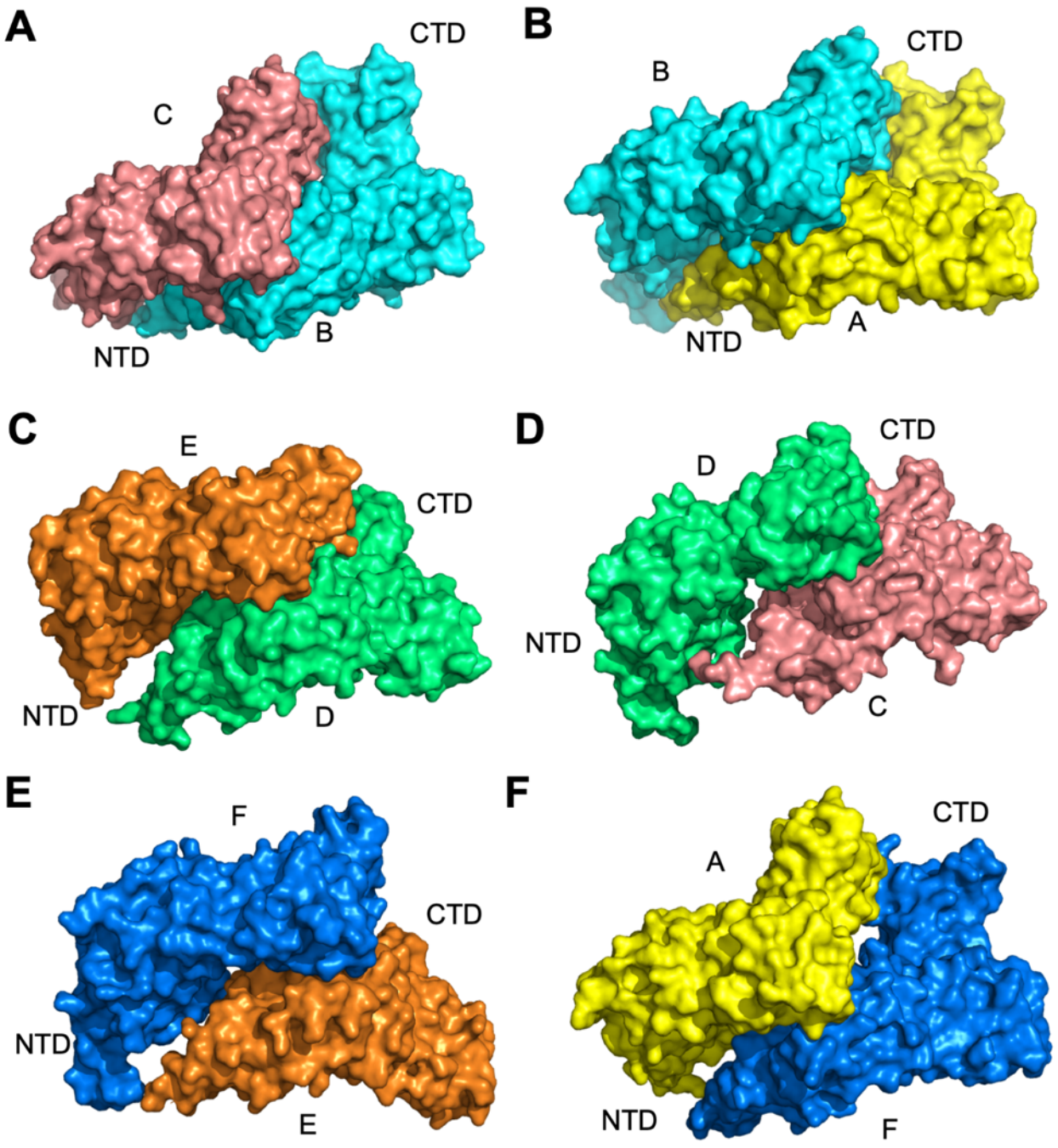

Fig. S7 Surface Representation of RuvB Dimers.
Surface representation of RuvB dimers BC (A), AB (B), DE (C), CD (D), EF (E), and FA (F) with protomers A, B, C, D, E, F colored in yellow, cyan, salmon, green, orange, and blue, respectively

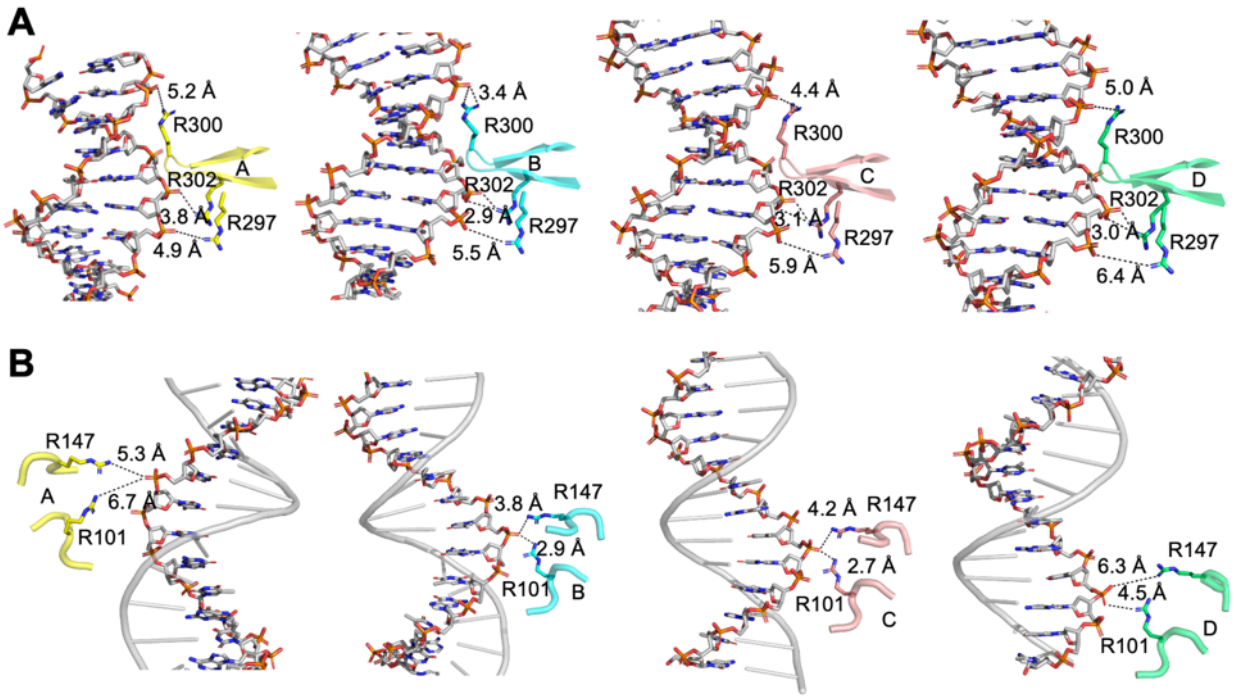

Fig. S8 Detained Interactions between RuvB and dsDNA.
(A) Ribbon diagram showing detailed interactions between Arg297, Arg300, Arg302, and DNA backbone with distances between arginine residues and phosphate groups labeled. (B) Ribbon diagram showing detailed interactions between Arg101, Arg147, and DNA backbone with distances between arginine residues and phosphate groups labeled.

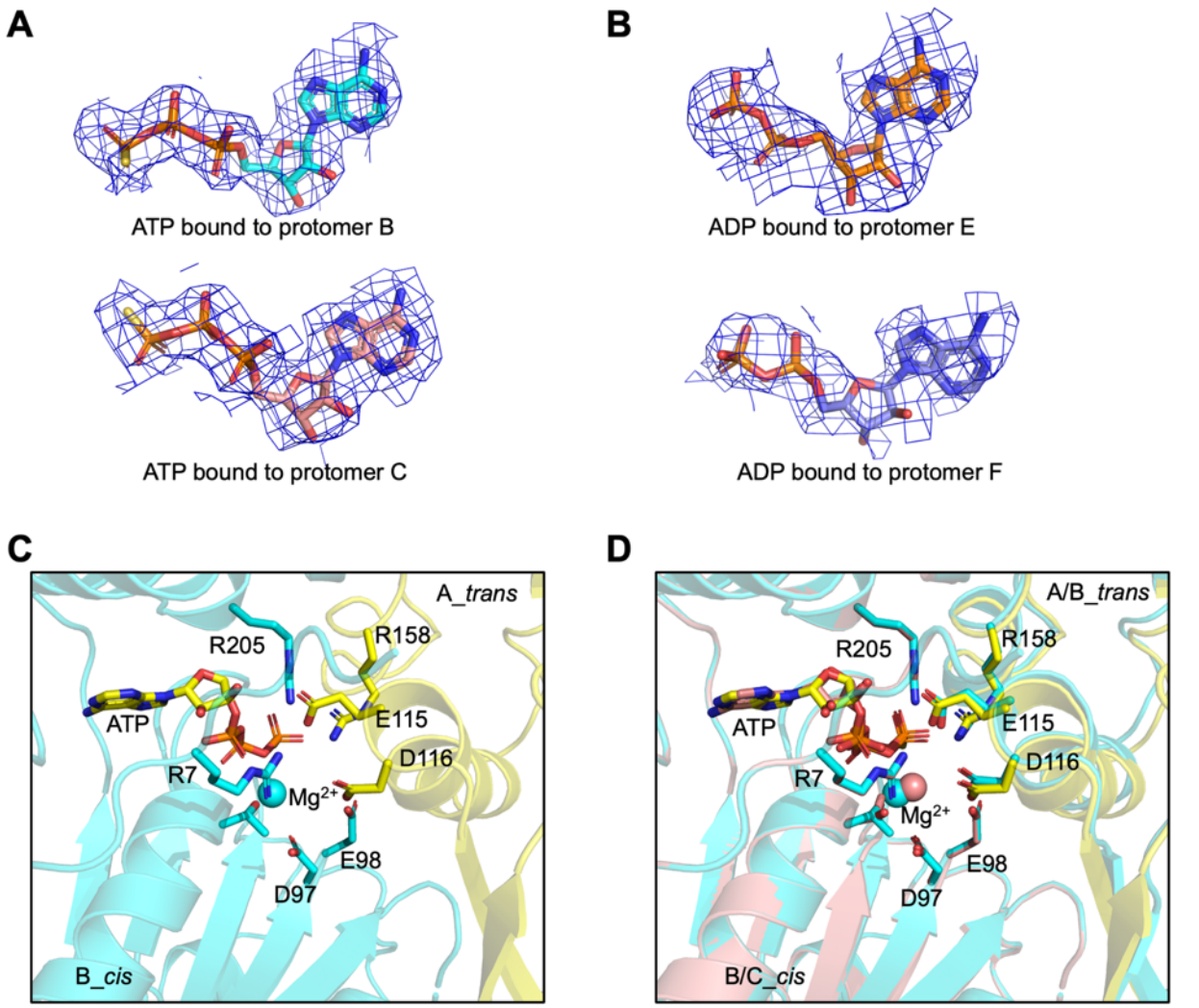

Fig. S9 Nucleotides and ATP Catalytic Centers in RuvB.
(A) ATP fitted to the cryo-EM density maps in protomers B and C at 2.0 **σ**.
(B) ADP fitted to the cryo-EM density maps in protomers E and F at 2.0 **σ**.
(C) The ATP catalytic center in the BA dimer with key residues for catalysis highlighted as sticks. Protomers B and A are shown in cyan and yellow, respectively.
(D) Comparison of the ATP catalytic centers in the BA dimer and the CB dimer, revealing similar conformations. Mg^{2+} ions shown as spheres.

Movie S1: Mechanisms of DNA translocation by the RuvB hexamer.

Table S1. Cryo-EM data collection, refinement, and validation statistics

Structures	RuvB hexamer	RuvB dodecamer
EMDB ID	28101	28107
Magnification	81,000	
Voltage (kV)	300	
Electron exposure (e–/Å^2)	50.0	
Defocus range (μm)	-0.5 to -2.5	
Pixel size (Å)	1.08	
Symmetry imposed	C1	C2
Initial particles (no.)	6,874,881	
Final particles (no.)	695,592	326,270
Map resolution (Å) FSC threshold	2.97 0.143	3.16 0.143
Models		
PDB ID	8EFV	8EFY
Initial model used (PDB)	1HQC	1HQC
Map sharpening *B* factor (Å^2)	-127.6	-138.2
Model composition Non-hydrogen atoms Protein residues Ligands	 15295 1944 6	 31274 3888 12
R.m.s. deviations Bond lengths (Å) Bond angles (°)	 0.003 0.564	 0.004 0.587
Validation MolProbity score Clashscore Poor rotamers (%)	 1.68 7.07 0.00	 1.69 7.33 0.00
Ramachandran plot Favored (%) Allowed (%) Disallowed (%)	 95.81 4.19 0.00	 95.78 4.22 0.00